Role of the Two Structural Domains from the Periplasmic *Escherichia coli* Histidine-binding Protein HisJ*

Byron C. H. Chu, Timothy DeWolf, and Hans J. Vogel[1]

From the Biochemistry Research Group, Department of Biological Sciences, University of Calgary, Alberta T2N 1N4, Canada

Background: HisJ is a bilobal periplasmic binding protein that mediates basic amino acid transport.
Results: The apo-HisJ solution NMR structure was solved. The individual lobes of HisJ were isolated, and domain 1 binds histidine.
Conclusion: Histidine binding at domain 1 initiates large conformational changes in HisJ.
Significance: Intact hinge regions that bridge the two lobes of HisJ are critical for function.

Escherichia coli **HisJ is a type II periplasmic binding protein that functions to reversibly capture histidine and transfer it to its cognate inner membrane ABC permease. Here, we used NMR spectroscopy to determine the structure of apo-HisJ (26.5 kDa) in solution. HisJ is a bilobal protein in which domain 1 (D1) is made up of two noncontiguous subdomains, and domain 2 (D2) is expressed as the inner domain. To better understand the roles of D1 and D2, we have isolated and characterized each domain separately. Structurally, D1 closely resembles its homologous domain in apo- and holo-HisJ, whereas D2 is more similar to the holo-form. NMR relaxation experiments reveal that HisJ becomes more ordered upon ligand binding, whereas isolated D2 experiences a significant reduction in slower (millisecond to microsecond) motions compared with the homologous domain in apo-HisJ. NMR titrations reveal that D1 is able to bind histidine in a similar manner as full-length HisJ, albeit with lower affinity. Unexpectedly, isolated D1 and D2 do not interact with each other in the presence or absence of histidine, which indicates the importance of intact interdomain-connecting elements (*i.e.* hinge regions) for HisJ functioning. Our results shed light on the binding mechanism of type II periplasmic binding proteins where ligand is initially bound by D1, and D2 plays a supporting role in this dynamic process.**

Periplasmic binding proteins (PBPs)[2] were originally identified as a class of proteins located near the surface of Gram-negative bacteria, which are released by mild osmotic shock and are able to bind a variety of small molecules (1, 2). PBPs are directly involved in the acquisition of nutrients such as phosphate, sulfate, some carbohydrates, and amino acids. Uptake of amino acids is important for bacteria as they contribute to the cytoplasmic amino acid pool (without the need for *de novo* biosynthesis) and are incorporated during protein translation. In Gram-negative bacteria basic amino acids can be transported across the outer membrane through general or specific porins such as OmpF or LamB. In *Escherichia coli*, once histidine gains access to the periplasm it can be transported into the cytoplasm via low and high affinity uptake systems. The low affinity system is known as the general aromatic transport system, and it is only able to transport histidine at concentrations of >0.1 mM through its cytoplasmic membrane permease, AroP (3). The high affinity histidine system is composed of the histidine-binding protein (HisJ), a PBP, and a permease (HisQMP$_2$). HisQM is a heterodimer that forms the integral membrane portion of the permease, and the HisP homodimer is the cognate cytoplasmic ATP-binding subunit (4). HisJ is able to bind histidine with high affinity ($K_d \sim 30$ nM) (5, 6) and deliver it to HisQMP$_2$ from where it is then translocated into the cytoplasm in an ATP-dependent manner. A second PBP, the lysine-, arginine-, and ornithine-binding protein (LAOBP), which shares 70% sequence identity with HisJ, is also able to serve HisQMP$_2$ and binds histidine with an $\sim$16-fold lower affinity than HisJ (7).

PBPs are distinguished based on their ligand specificity and structural features such as the number of interdomain cross-links (*i.e.* hinge regions) (8–13). In types I, II, and III PBPs, the two structural domains are connected by three, two, and one hinge regions, respectively. By-products of having multiple hinge regions are the structural domains that are folded discontinuously. For example, in the type II PBP HisJ, domain 1 (D1) is formed by two subdomains where one (D1A) is folded first, then domain 2 (D2), and finally the second subdomain (D1B) of D1 (Fig. 1*A*). The apo-forms of type II PBPs (*e.g.* LAOBP- and glutamine-binding protein) (14–16) have been crystallized in an open conformation wherein there are few interdomain contacts except for regions adjacent to the hinge regions. For these PBPs, ligand binding occurs in the interdomain cleft region and is accompanied by significant closing and twisting motions that bring the domains together (14, 17). Although no structure for apo-HisJ has previously been reported, it is expected to adopt

[2] The abbreviations used are: PBP, periplasmic binding protein; CSI, Chemical Shift Index; CSP, chemical shift perturbation; D1, domain 1; D2, domain 2; HSQC, heteronuclear single quantum coherence; LAOBP, lysine, arginine, ornithine binding protein; MBP, maltose binding protein; MD, molecular dynamics; PDB, Protein Data Bank; RDC, residual dipolar coupling; TEV, tobacco etch virus; CPMG, Carr-Purcell-Meiboom-Gill; ITC, Isothermal titration calorimetry.
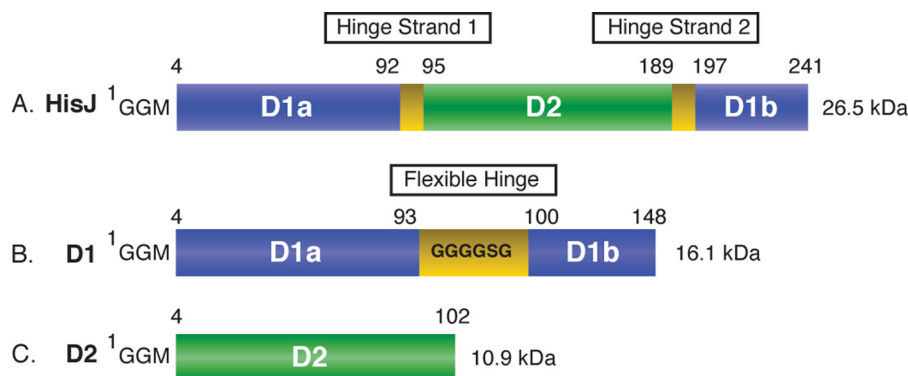
FIGURE 1. **Schematic diagram of the protein constructs used in this study.** The numbering for the HisJ (*A*), D1 (*B*), and D2 (*C*) constructs is indicated and includes the N-terminal GGM extension that is a remnant of the purification procedure. D1, D2, and hinge strand residues are colored *blue, green,* and *yellow*, respectively.

an open conformation similar to the related LAOBP protein (18–22). Two crystal structures for HisJ complexed with histidine have been solved for the proteins from *E. coli* (PDB 1HSL) (23) and *Salmonella typhimurium* (PDB 1HPB) (24) whose sequences are essentially identical (98.3%), except for four residues that are not directly involved in function. Holo-HisJ adopts a closed conformation similar to that of LAOBP bound to various ligands (14).

In this work, we solved the solution structure for apo-HisJ in an open conformation and also confirmed that the structure of the holoprotein in aqueous solution closely resembles that in the crystal structures. We then examined the type and strength of interactions that mediate domain-domain interactions in the HisJ protein using NMR as our primary investigative tool. Our approach was to dissect this protein by expressing each domain individually and to perform protein interaction studies with them in the absence of interdomain connectivity. Our results support the idea that the individual domains of HisJ retain the same global fold as in the WT protein; however, there are apparent functional differences related to the absence of an intact hinge region. The two domains of HisJ were unable to interact in the absence of ligand; moreover, in the presence of histidine only D1 was found to bind histidine. These results strongly support the idea that ligand binding is initiated by the D1 domain of HisJ and that the intact linker region is required for transmission of the "closing" signal to the D2 region.

EXPERIMENTAL PROCEDURES

Cloning of E. coli HisJ and Construct Generation—The mature HisJ protein (residues 1–238), without periplasmic signal sequence, was amplified from the *E. coli* K12 genome through PCR with oligonucleotides containing 5′-NdeI and 3′-XhoI (New England Biolabs) restriction sites and cloned into the pET15-MHL vector. Domain 1 (D1, residues 1–93 and 193–238) and domain 2 (D2, residues 94–192) constructs of HisJ are described in Fig. 1. For cloning of D1, subdomain A (residues 1–93) was amplified with oligonucleotides containing 5′-NdeI and 3′-KpnI restriction sites, whereas subdomain B (residues 193–238) was amplified with oligonucleotides containing 5′-KpnI and 3′-XhoI restriction sites. Subdomains A and B were digested with KpnI and ligated using T4 ligase (Fermentas). The newly created D1 construct was then amplified by

PCR and cloned into the pET15-MHL vector using the 5′-NdeI and 3′-XhoI restriction sites. A flexible linker (Gly-Gly-Gly-Gly-Ser-Gly) was inserted between subdomains A and B of D1 to prevent inadvertently constraining either subdomain in a non-native conformation (Fig. 1). The D2 construct was amplified by PCR and cloned into the pET15-MHL vector using the 5′-NdeI and 3′-XhoI restriction sites.

The pET15-MHL vector was kindly donated by the Structural Genomics Consortium (University of Toronto) and attaches a hexa-histidine tag and a tobacco etch virus (TEV) protease cleavage site to the N terminus of the expressed protein. Cleavage of the expressed protein with TEV protease results in the addition of Gly-Gly-Met to the N terminus. Constructs were verified through nucleotide sequencing at the University of Calgary Genetic Analysis Laboratory. Of note, the HisJ residue numbering in this study includes the additional three amino acids at the N terminus of the protein constructs and thus differs from the native HisJ sequence (*e.g.* Ala-4 of this paper is equivalent to Ala-1 of the native HisJ sequence).

Sample Preparation—For overexpression of HisJ, D1, and D2, *E. coli* BL21 (DE3) cells with the vector of interest were grown in 1 liter of Luria-Bertani (LB) in the presence of 100 μg/ml ampicillin. For NMR experiments, isotope-labeled HisJ, D1, and D2 were prepared using the general isotope-labeling strategy outlined by Tugarinov *et al.* (25) and Huang and Vogel (26). Briefly, *E. coli* BL21 cells (DE3) were grown in 1 liter of D_2O M9 medium containing 3 g/liter D-[U-^{1}H,^{13}C]glucose (Cambridge Isotope Laboratories) as the sole carbon source and 1 g/liter $^{15}NH_4Cl$ (Cambridge Isotope Laboratories) as the nitrogen source. Depending on the experiment and the protein, H_2O, M9 media and unlabeled D-glucose and NH_4Cl were used in place of their labeled counterparts. For HisJ and D2, cells were grown to an absorbance at 600 nm (A_{600}) of ~0.8 at 37 °C and induced with 0.8 mM isopropyl β-D-1-thiogalactopyranoside for 3 h. For expression of D1, cells were grown to an A_{600} of ~0.5 at 37 °C and induced with 0.5 mM isopropyl β-D-1-thiogalactopyranoside at room temperature for ~16 h. Cells were then harvested and resuspended in 20 mM Tris, 0.1 M NaCl, and 20 mM imidazole (pH 8) and lysed by a French pressure cell. The cell lysate was centrifuged at 18,500 × g for 45 min at 4 °C. Nickel affinity column chromatography was performed using

chelating Sepharose (GE Healthcare), where bound proteins were washed with 20 mM Tris, 0.1 M NaCl, and 20 mM imidazole (pH 8), and proteins were eluted with 20 mM Tris, 0.1 M NaCl, and 250 mM imidazole (pH 8). SDS-PAGE was used to confirm protein homogeneity. The purified proteins were then buffer exchanged into 20 mM Tris, 0.1 M NaCl, 0.5 mM EDTA, 3 mM L-glutathione (reduced; Sigma), and 0.3 mM (−)-glutathione (oxidized; Sigma (pH 8)) and subjected to TEV protease digestion (∼ 4 h at 30 °C) to remove the N-terminal histidine tag. The solution was then buffer exchanged into 20 mM Tris, 0.1 M NaCl (pH 8) and applied to a chelating Sepharose column where the cleaved histidine tag and TEV protease are bound, and histidine tag free HisJ, D1, and D2 are found in the flow-through. The proteins were subsequently dialyzed into 5 mM Tris (pH 8) for anion-exchange chromatography using a DEAE-Sepharose Resource Q column (GE Healthcare) and eluted with a linear gradient of 0.1 M NaCl in 5 mM Tris (pH 8). This final anion-exchange chromatography step was used to further purify the proteins and remove any bound histidine. The protein concentrations were determined through a theoretical extinction coefficient (ϵ_{280}) calculated using the ExPASy Prot-Param program. For D1, Bradford assays (27) were used to confirm the protein concentration determined by ϵ_{280}.

In general, protein samples were prepared in 50 mM Na_3PO_4 (pH 7). For NMR experiments, 0.5 mM 2,2-dimethyl-2-silapentane-5-sulfonate was added for peak referencing as well as 10% v/v D_2O. Holo-HisJ NMR samples were prepared by adding 5 mM histidine. NMR samples for backbone assignments of HisJ and D1 contained ∼1 mM U-^{13}C,^{15}N-^{1}H/^{2}H-labeled protein, although for D2 ∼1 mM ^{13}C,^{15}N-labeled protein was utilized. Methyl assignments for apo-HisJ were acquired on the same U-^{13}C,^{15}N-^{1}H/^{2}H-labeled sample as the backbone assignments according to Mulder and co-workers (28). ^{13}C,^{15}N-Labeled apo-HisJ (∼1 mM) was used in the acquisition of NOESY NMR experiments. NMR spin relaxation experiments were performed on ∼1 mM U-^{15}N-^{1}H/^{2}H-HisJ and -D1 and ∼1 mM ^{15}N-labeled D2. Residual dipolar coupling (RDC) experiments were performed using the same labeling scheme as the NMR spin relaxation experiment samples except that ∼0.5 mM protein was used, and 150 mM NaCl was added to the buffer. RDC experiments for holo-HisJ were performed with 50 mM NaCl to prevent disruption of histidine binding (6). NMR titration experiments were performed with ∼0.3 mM ^{15}N-D1 or -D2 and with 100 mM NaCl. Of note, unless otherwise specified, histidine refers to L-histidine.

ITC Experiments—All ITC experiments were performed using a Microcal VP-ITC microcalorimeter (GE Healthcare). All samples were prepared in a buffer containing 20 mM HEPES (pH 7.0) and 100 mM NaCl. The syringe was filled with 0.5 mM histidine that was injected into the ITC cell containing 20 μM protein (D1, D2, or HisJ) solution at 30 °C. The heat of dilution was measured separately by injecting titrant into the ITC buffer and was shown to be negligible. After subtraction of the heat of dilution, the data were fit to a one-site binding model (MicroCal Origin version 7.0 software) to obtain the stoichiometry (N), enthalpy (ΔH), and association constant (K_a), which are converted to K_d values using the relationship shown in Equation 1,

$$K_d = 1/K_a \tag{Eq. 1}$$

and where the reported values are the average and S.D. of three independent titrations.

NMR Experiments—All NMR experiments for the backbone chemical shift assignments, titrations, and relaxation experiments were performed at 298 K on Bruker Avance 500- or 700-MHz NMR spectrometers equipped with triple resonance inverse cryoprobes with a single axis z-gradient. Sequential assignments of H^N, N, C′, C^{α}, and C^{β} resonances of apo- and holo-HisJ, D1, and D2 were achieved using two-dimensional ^{1}H,^{15}N-HSQC and three-dimensional HNCACB, HN(CO)CACB, HN(CA)CO, and HNCO experiments. For apo- and holo-HisJ and D1 proteins, TROSY versions of these experiments were used (29, 30). For apo-HisJ, methyl group assignments were acquired using a three-dimensional C-TOCSY-CHD$_2$ experiment (28). NMR chemical shift assignments for apo-, holo-, D1-, and D2-HisJ have been deposited in the Biological Magnetic Resonance Data Bank (BioMagResBank) under the accession codes 19242, 19245, 19243, and 19244, respectively.

NMR spin relaxation experiments were conducted at a static magnetic field strength of 500 MHz on [U-^{15}N]^{1}H/^{2}H apo- and holo-HisJ and ^{15}N-D1 and -D2 samples. ^{15}N R_1 values were performed using sensitivity-enhanced inversion-recovery pulse sequences (31) with T delays of 14, 70, 210, 420, 560 (2×), 700 (2×), 882, and 1060 ms. ^{15}N R_2 values were acquired using sensitivity-enhanced Carr-Purcell-Meiboom-Gill (CPMG)-type T_2 experiments with pulsed field gradients (31), with T delays of 8 (2×), 16 (2×), 40, 48, 64 (2×), 72, 80, and 96 ms. {^{1}H} ^{15}N NOE experiments were recorded with and without a ^{1}H presaturation period of 5 s and an interscan delay of 5 s. Relaxation dispersion experiments were performed with TROSY-based CPMG experiments at 50.684 MHz for the ^{15}N frequency (32, 33). CPMG spectra were acquired at frequencies (ν_{CPMG}) of 40 and 1000 Hz. The NMR relaxation dispersion ($R_{2\ eff}$) was calculated as shown in Equation 2,

$$R_{2\ eff}(\nu_{CPMG}) = (-1/T_{CP})\ln(I_{\nu\ CPMG}/I_o) \tag{Eq. 2}$$

A mixing time of 120 ms was used in the three-dimensional ^{15}N-edited NOESY-TROSY (34) and constant time ^{13}C-edited NOESY-HSQC experiment acquired on a ^{13}C,^{15}N-apo-HisJ sample. NOESY experiments were collected using a nonuniform sampling procedure (30%) where processing was performed by MDDGUI 1.0 software (Arrowsmith Laboratory, University Health Network, University of Toronto), which requires MddNMR 2.0 (35). The ^{13}C-edited NOESY-HMQC was acquired in 99.9% D_2O.

$^{1}D_{NH}$ RDC were measured on partially aligned U-^{15}N-^{1}H/^{2}H apo- and holo-HisJ and ^{15}N-D1 and -D2 samples. The alignment media used included Pf1 phage (Asla Lab) at concentrations of 10 mg/ml for apo- and holo-HisJ and 12 mg/ml for D1 and D2 (36). $^{1}D_{NH}$ RDCs were measured using an in-phase/anti-phase ^{1}H,^{15}N-HSQC experiment with 2048 × 512 complex points (37). The PALES (38) software was used to fit the measured H^N-N RDCs to those back-calculated from the crystal structure of the holo-(histidine) HisJ complex (PDB 1HSL) and models of D1 and D2 built from the apo- and holo-HisJ

structures. Of note, the deposited holo-HisJ structure (1HSL) contains four point mutations (N5K, S22A, E107A, and S184A) that were corrected to match the HisJ sequence from *E. coli* K12 (GenBank™ accession number BAA16155.1) using MODELLER (39) prior to analysis. Only well structured regions of D1, D2, and HisJ were chosen for analysis based on {¹H} ¹⁵N NOE values >0.65 from NMR spin relaxation experiments (see below).

CSPs upon ligand binding were examined on a per residue basis using a combined chemical shift difference, where applicable, according to Mulder *et al.* (40) for backbone atoms, where R_i denotes the scaling factor of nucleus i. The scaling factors used were $R_N = 6.4$, $R_{C'} = 3.0$, R_C^α, and $R_C^\beta = 3.2$ as shown in Equation 3.

$$\Delta\delta_{bb}(ppm) = (\Delta\delta_{HN}^2 + (\Delta\delta_N/R_N)^2 + (\Delta\delta_{C'}/R_{C'})^2 + (\Delta\delta_C^\alpha/R_C^\alpha)^2 + (\Delta\delta_C^\beta/R_C^\beta)^2)^{1/2} \quad \text{(Eq. 3)}$$

All data were processed with the NMRPipe (41) software package and analyzed using the program Sparky (42). Protein backbone dihedral angle data were calculated using the program TALOS+ (43), and all chemical shifts were referenced to 2,2-dimethyl-2-silapentane-5-sulfonate (44).

NMR Analysis—For NMR spin relaxation experiments, the values of R_1 and R_2 were obtained by fitting the extracted peak intensities to a mono-exponential decay curve. Peak intensities were extracted using the relaxation module in Sparky (42), and data fitting was performed by Curvefit version 1.4 (A. G. Palmer, Columbia University) using the script "sparky2rate." Uncertainties in the peak heights were determined from duplicate measurements, and uncertainties in R_1 and R_2 were estimated from Jackknife simulations (45). {¹H} ¹⁵N NOE values were determined from the experiments with and without irradiation. Data points with errors larger than 25% were excluded from the analysis. Relaxation data used in the rotational diffusion analysis were subject to filtering as described by Bax and co-workers (46) The rotational correlation time for the global tumbling (τ_m) of each residue was estimated from R_2/R_1 ratio using the program R2R1_tm (A. G. Palmer, Columbia University), and the overall rotational correlation times (τ_c) were determined by averaging the per residue τ_m values.

Apo-HisJ Structure Calculation—An initial template apo-HisJ structure was generated by threading the HisJ sequence onto the apo-LAOBP structure (PDB 2LAO) using Swiss-Model (47). For the structure calculation, deuterium isotope-corrected backbone chemical shifts (48, 49) were used to determine the position of secondary structure elements and dihedral backbone angle (Φ,Ψ) (43) values utilizing the programs chemical shift index (CSI) (50) and TALOS+ (43), respectively. Of note, TALOS+ restraints were used for all residues except proline. Secondary structure elements were implemented in structure calculations using artificial hydrogen bond restraints according to Tugarinov *et al.* (51). RDC (52, 53) and distance restraints were also used as input for the structure calculations. Distance restraints were binned according to Tugarinov *et al.* (51), where the majority of H^N-H^N NOEs were bound to 1.8–5.0 Å, except for residues in helices (1.8–4.0 Å). CH₃-CH₃ and CH₃-H^N NOEs were binned to 1.8–8.0 and 1.8–6.0 Å, respectively, except for intraresidue H^N-CH₃ NOEs (1.8–4.0 Å). Apo-

HisJ structures were calculated with Xplor-NIH software (54), using torsion angle simulated annealing according to a two-stage, low temperature protocol (55–57). In stage 1, the starting model undergoes Powell energy minimization, 10 ps of torsion angle dynamics (at 200 K), and 4 ps of simulated annealing at each step wherein the temperature was incrementally decreased from 200 to 20 K at a 10 K step size. During simulated annealing, the force constants were increased except the backbone torsion angle restraints for φ and ψ, which are fixed at 300 kcal mol⁻¹ rad⁻². 200 structures were generated in stage 1, and the lowest energy structure was selected as the starting model for the next stage. Stage 2 involves 10 ps of torsion angle dynamics at 20 K, which is followed by 6 ps of simulated annealing at each temperature step from 20 to 1 K in 1 K increments. In stage 2, the backbone dihedral angle force constant was ramped down from 300 to 50 kcal mol⁻¹ rad⁻², and the backbone angle restraints were derived from the lowest energy structure from stage 1. 100 structures were calculated in stage 2, and an ensemble of the 30 lowest energy structures was generated and validated using the program Protein Structure Validation Suite (58). The atomic coordinates for the 30 lowest energy structure ensemble of apo-HisJ has been deposited in the PDB under the accession code 2M8C. All molecular graphics were created using PyMOL (59).

RESULTS

NMR Characterization—The domains of HisJ were cloned, expressed, and characterized in order to assess their global folds and to examine their ability to interact with each other in the presence or absence of ligand. ¹H-¹⁵N (TROSY) HSQC spectra of all protein constructs used in this study show well folded structures (Fig. 2). From the backbone experiments, 99.7% of all possible ¹H^N, ¹⁵N, ¹³Cα, ¹³Cβ, and ¹³C' resonance assignments for both apo- and holo-HisJ (complexed with histidine) were assigned. In both proteins, the ¹H^N, ¹⁵N, and ¹³Cβ resonance assignments of Ser-25 could not be determined. The overall completeness of the backbone resonance assignment for apo-HisJ represents a slight improvement from a previously published NMR assignment (60). In particular, apo-HisJ backbone amide resonances for Ile-59, Ser-72–Gln-81, Gln-146, and Lys-228 could be resolved through the use of perdeuteration and TROSY (29). The backbone resonance assignments for the D1 and D2 constructs were also assigned to near-completeness at 99.4 and 97.8%, respectively. For D1, the missing assignments belonged to residues Ser-25 and Glu-78 (¹H^N and ¹⁵N). For D2, the missing assignments included Asn-12 and Thr-34 (¹H^N and ¹⁵N) and Pro-17 ¹³Cβ.

Using a two-stage low temperature simulated annealing protocol, the apo-HisJ NMR structure was determined in an open conformation where the two lobes of the protein are spread apart (Fig. 3A; Table 1). Similar to other PBPs, each lobe of HisJ displays a mixed α/β-fold (Rossmann-like) characterized by a central β-sheet (61). In contrast, the holo-HisJ crystal structure (PDB 1HSL; Fig. 3B) displays a closed conformation with the two lobes making extensive interdomain contacts. Comparison of the apo- and holo-HisJ forms using combined backbone CSP analysis reveals several regions with large values (Fig. 3C) that can be attributed to the conformational transition that occurs
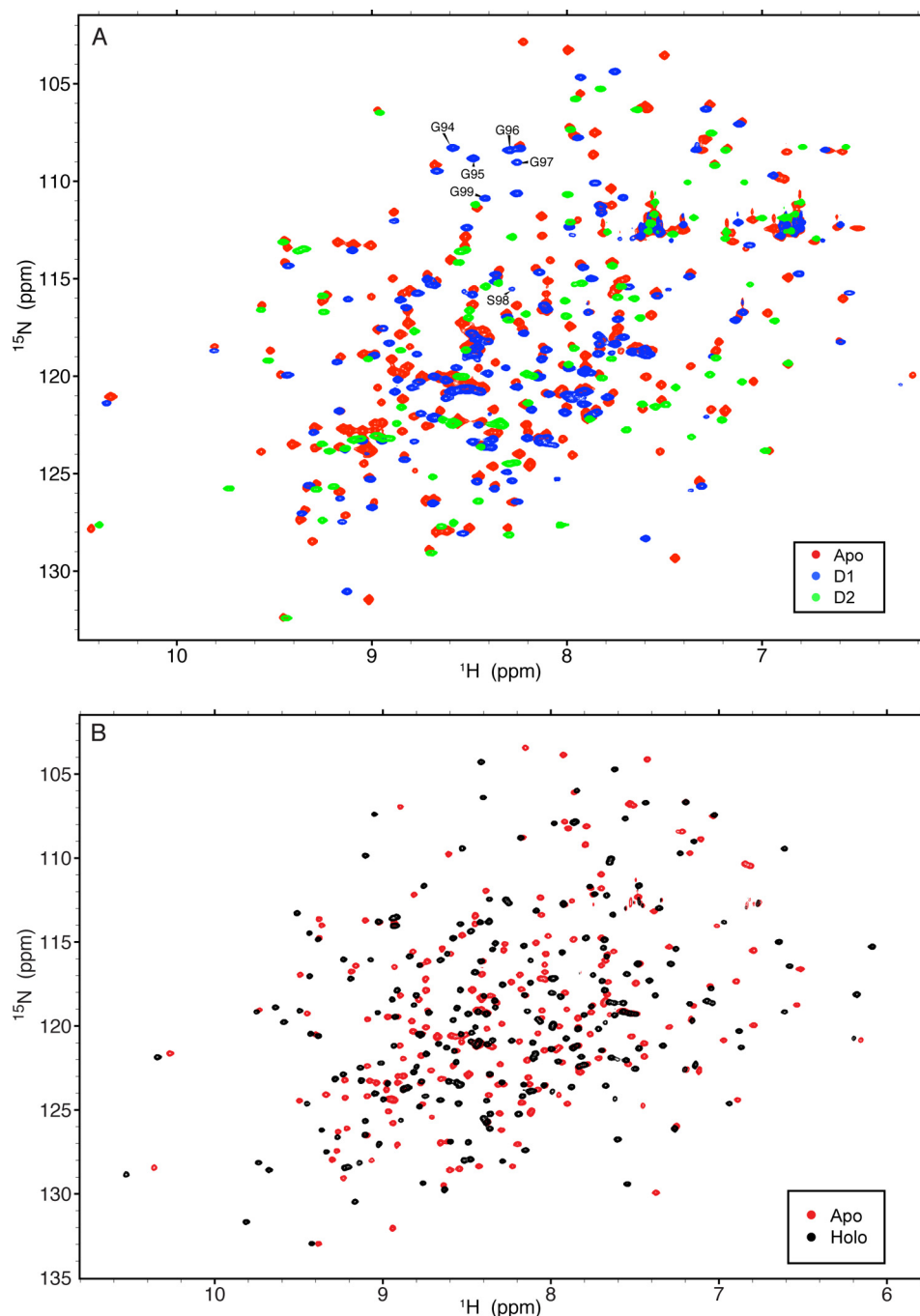
FIGURE 2. **^{1}H,^{15}N (TROSY) HSQC spectra of protein constructs from this study.** *A,* ^{1}H,^{15}N-HSQC NMR spectra of ^{2}H,^{15}N-apo-HisJ (*red*), ^{15}N-D1 (*blue*), and ^{15}N-D2 (*green*) protein constructs. Residues from the inserted flexible linker region of D1 are labeled. *B,* ^{1}H,^{15}N TROSY-HSQC spectra of ^{2}H,^{15}N-apo-HisJ (*red*) and ^{2}H,^{15}N-holo-HisJ (*black*).

upon ligand binding as well as modifications to the chemical environment of ligand-interacting residues.

CSPs indicate that the chemical environments of the individual H^N-N chemical shifts from D1 and D2 compare favorably with those of apo-HisJ (Fig. 4*A*). For the D1 protein, significant CSPs for residues 93 and 100–104 were observed. These residues are located adjacent to the artificial D1 linker and are part of the two interdomain linkers (residues 92–95 and 189–197) in the full-length HisJ constructs. For D2, residues at the N′ and C′ termini experience significant (>1 S.D.) CSPs, as well as residues 73, 76–77, and 79–83 that correspond to residues 163,

166–167, and 169–173, respectively, in the full-length protein (Fig. 4*A*). Despite these differences, the majority of the domain chemical shifts compare favorably with those from apo-HisJ. Similarly, analysis of calculated backbone dihedral angles (Φ and Ψ) reveals large changes at regions adjacent to the flexible D1 linker and termini regions of D2 compared with apo-HisJ (Fig. 4*B*).

Secondary structure distribution as determined by the CSI (50) data reveals that both apo- and holo-HisJ have similar composition and distribution of secondary structure elements (Fig. 4, *C* and *D*). Furthermore, secondary structure element distri-
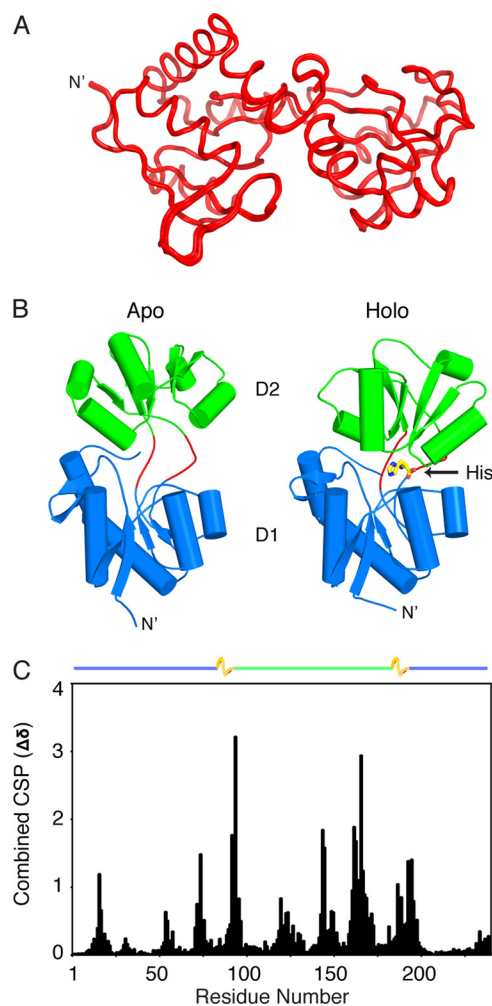
FIGURE 3. **NMR structure of apo-HisJ.** *A*, 30 lowest energy structures of apo-HisJ (*red*) overlaid (see Table 1 for structural statistics). *B*, side-by-side comparison of the lowest energy NMR structure of apo-HisJ and the crystal structure of holo-HisJ (PDB 1HSL). The first (D1) and second domain (D2) of each structure is colored *blue* and *green*, respectively. Holo-HisJ adopts a closed conformation in comparison with apo-HisJ, which results in histidine (*yellow*) being engulfed. Of note, hinge regions are colored *red*. *C*, combined NMR CSP for apo-HisJ and holo-HisJ (complexed with histidine). The domain organization of HisJ is noted *above* the figure where D1 subdomains (*blue*), D2 (*green*), and hinge regions (*yellow*) are indicated.
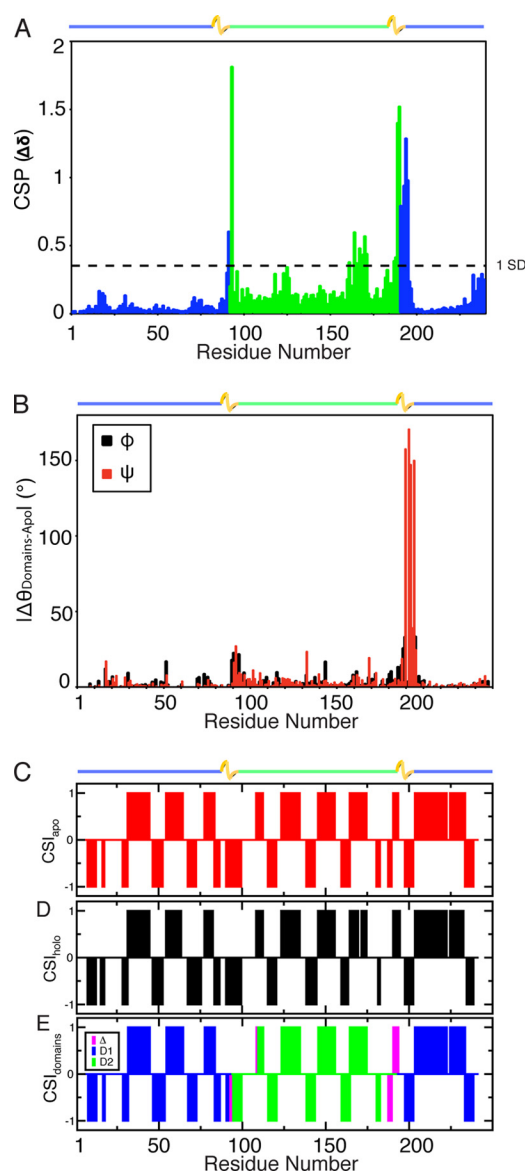
TABLE 1

Experimental restraints and structural statistics for the 30 lowest total energy structures of apo-HisJ

r.m.s.d. means root mean square deviation.

No. of experimental restraints	
Upper distance restraints from NOE	
Total	1370
Short/medium range	917
Long range	453
$^1D_{NH}$ RDCs	185
Dihedral angle restraints (TALOS+)	407
Hydrogen bonding restraints	74
Average r.m.s.d. values from experimental data	
Distance restraint violation	0.065 Å
Dihedral angle restraint violation	0.217°
RDC restraint violation	0.104 Hz
Average r.m.s.d. values from idealized covalent geometry	
Bonds	0.003 Å
Angles	0.434°
Impropers	0.444°
PROCHECK Ramachandran analysis for the folded regions	
Residues in most favored regions	84.8%
Residues in additional allowed regions	13.5%
Residues in generously allowed regions	1.7%
Residues in disallowed regions	0%
Coordinate precision of folded regions	
Backbone	0.13 ± 0.06 Å
All heavy atoms	0.18 ± 0.06 Å

adopts an open conformation, which was later confirmed with our NMR structure. Holo-HisJ H^N-N RDCs have a high degree of agreement with the closed conformation holo-HisJ crystal structure (PDB 1HSL; Fig. 5*B*), whereas D1 H^N-N RDCs have similar levels of correlation with domains from either the apo-open or holo-closed HisJ structures (Table 2; Fig. 5*C*). Interestingly, D2 H^N-N RDCs have a higher correlation with the equivalent domain in the holo-HisJ crystal structure than the apo-HisJ NMR structure (Fig. 5*D*). These RDC results indicate that the D1 and D2 H^N-N bond vectors closely resemble those found in the apo-open and holo-closed HisJ structures; however, D2 shows greater differences with respect to the apo-form of which Ser-97 (full-length Ser-187) has the largest variation (Fig. 5*E*).

NMR Spin Relaxation—NMR relaxation experiments (R_1, R_2, and {^1H} ^{15}N NOE) can provide information on protein tumbling and dynamics on the picosecond to nanosecond time scale. Apo- and holo-HisJ are rigid proteins with highly flexible terminal regions (residues 1–8 and 241; Fig. 6*A*). Compared with the holo-form, apo-HisJ has increased flexibility at Gly-145 and residues 196 and 197 from the 2nd interdomain linker. Furthermore, residues 93 and 95 of apo-HisJ have broadened peak line widths compared with their holo-form counterparts suggesting an increase in conformational averaging perhaps due to increased dynamics. D1 has increased mobility at the N′- and C′-terminal ends as well as the Gly linker region (residues 94–99) but is otherwise rigid (Fig. 6*B*). Similar to apo-HisJ, D2 behaves as a globular rigid protein except for residue Gly-55 (corresponding to full-length Gly-145) and the N′- and C′-terminal residues (Fig. 6*C*). Rotational diffusion analysis of the R_1 and R_2 data allowed for calculations of average rotational correlation times (τ_c) from the τ_m values of each residue. Apo- and holo-HisJ (26.5 kDa) have similar correlation times of 13.83 ± 1.12 and 13.79 ± 1.23 ns (Fig. 6*D*), respectively,

bution of the solution holo-HisJ protein compares favorably to that of the *E. coli* holo (histidine)-HisJ crystal structure (PDB 1HSL, data not shown). Comparison of CSI predictions for D1 and D2 *versus* the full-length apo-HisJ protein reveals an almost perfect level of conservation except for residues immediately adjacent to the D1 flexible linker and at the N′ and C′ termini of D2 (Fig. 4*E*).

H^N-N RDCs were used to assess the folding of D1 and D2 and examine the orientations of these domains in holo-HisJ. H^N-N RDCs provide information on the average orientation of interatomic H^N-N vectors relative to the molecular alignment tensor (52). The RDC is used to define the H^N-N bond vector with respect to the external magnetic field and can be used to assess domain orientation (62). The high degree of correlation between the measured H^N-N RDCs for apo-HisJ and those back-calculated from the initial starting model (see "Experimental Procedures"; Table 2; Fig. 5*A*) suggested that apo-HisJ

FIGURE 4. **Structural similarity of the isolated domain constructs and their equivalent domains in apo-HisJ.** *A,* H^N-N CSP of D1 (*blue*) and D2 (*green*) compared with apo-HisJ. The *horizontal line* indicates CSPs greater than 1.0 S.D. from the mean. *B,* comparison of the backbone dihedral angles of D1 and D2 *versus* apo-HisJ that were calculated using the program TALOS+. *C* and *D,* CSI secondary structure prediction results for apo- and holo-HisJ, respectively. *E,* CSI results for D1 (*blue*) and D2 (*green*). Residues where differences in secondary structure (compared with apo-HisJ) are detected are colored *purple*. CSI results are interpreted as +1 for α-helical propensity, −1 for β-strand prediction, and 0 for random coil. Of note, the inserted flexible linker of D1 was excluded in the comparison. The domain organization of HisJ is noted *above* the figures.

TABLE 2

RDC analysis of H^N-N bond vectors from apo- and holo-HisJ and D1 and D2

Experimental values are compared with those back-calculated from the structures of apo- and holo-HisJ. A high *R* value and a low *Q* value indicate close agreement.

Protein	No. of residues	Structure	R	Q
				%
Apo-HisJ	184	Apo-open (starting model)	0.95	0.30
	184	Holo-closed (PDB 1HSL)	0.78	0.63
Holo-HisJ	202	Apo-open (NMR)	0.80	0.60
	202	Holo-closed (PDB 1HSL)	0.94	0.34
D1	115	D1 model (apo-NMR)	0.94	0.34
	115	D1 model (holo-crystal)	0.95	0.30
D2	82	D2 model (apo-NMR)	0.83	0.56
	82	D2 model (holo-crystal)	0.94	0.36

CPMG relaxation dispersion experiments indicate areas that are involved in slow chemical exchange (millisecond to microsecond). Relaxation dispersion data indicate that apo-HisJ experiences slow conformational motions, although holo-HisJ does not (Fig. 7*A*). From the D1 domain of apo-HisJ, Ala-18 undergoes elevated ($R_{2 \text{ eff } 40 \text{ Hz}/1000 \text{ Hz}} = 2.0$) slow motions and residues 98, 197, and 198 located proximal to the hinge regions also experience significant dispersion ($R_{2 \text{ eff } 40 \text{ Hz}/1000 \text{ Hz}} > 1.3$). Residues 121, 125, 151, 152, 161, 163, 171, and 174 from the D2 domain of apo-HisJ also show significant slow motions. The majority of the residues experiencing chemical exchange occurs in the D2 region of apo-HisJ, although nearly all of the D1 $R_{2 \text{ eff}}$ ratios remain unperturbed. Isolated D1 experiences no significant chemical exchange (Fig. 7*B*), whereas residues in the latter portion of D2 show elevated $R_{2 \text{ eff}}$ values (>1.25), including C-terminal Lys-102 ($R_{2 \text{ eff}} = 1.53$; Fig. 7*C*). Overall, isolated D2 residues (8, 31, 35, 61, 71, 73, and 81) experience a significant reduction in slow motions compared with the equivalent residues in apo-HisJ.

Ligand Binding—Previous studies have established that HisJ binds histidine with a higher affinity than other basic amino acids (5, 6, 21, 63, 64). ITC and NMR were used to examine the binding of histidine to apo-HisJ, D1, and D2. Apo-HisJ exhibited an exothermic interaction with histidine with a binding constant (K_d) of 114 ± 16 nM using ITC (Fig. 8). The thermodynamic parameters for histidine binding to HisJ are $\Delta H = -61.2 \pm 0.126$ kJ/mol and $T\Delta S = -23 \pm 0.412$ kJ/mol, which indicate that it is driven by a favorable enthalpy term. Binding constants and thermodynamics of histidine binding to D1 and D2 could not be determined as the molecules did not interact, the interaction was too weak to be detected, or the reaction did not produce a discernable heat signal (data not shown). NMR titrations were performed to examine CSP changes in the HSQC spectra of D1 and D2 upon addition of histidine. Based on the apo-HisJ NMR titration with histidine (Fig. 3*C*), it was expected that many CSPs would be observed in the experiments with the isolated domains. In the D1 titration, a small number of signals shift in a fast exchange manner (on the NMR time scale) upon histidine addition, which indicates weak binding (K_d Ser-73 ∼80 μM; Fig. 9, *A* and *B*). In the isolated D2 NMR titration, no significant CSPs were observed suggesting that D2 is not able to bind histidine (Fig. 9*C*), which is consistent with the ITC results. From the *E. coli* HisJ crystal structure (PDB 1HSL), both D1 and D2 residues make direct contact with the histidine ligand (Table 3). The majority of these

despite the difference in conformation. The D1 and D2 domains within the apo- and holo-HisJ proteins have similar τ_c values suggesting that the domains tumble dependently in solution. Isolated D1 and D2 have correlation times of 8.59 ± 0.36 and 5.33 ± 0.31 ns, respectively, indicating that these proteins tumble as monomers in solution (Fig. 6, *E* and *F*). For D1, measurement of similar τ_c values for D1a and D1b subdomains indicate that they tumble dependently and provide further evidence to suggest that D1 is folded similarly to the D1 domain within HisJ.
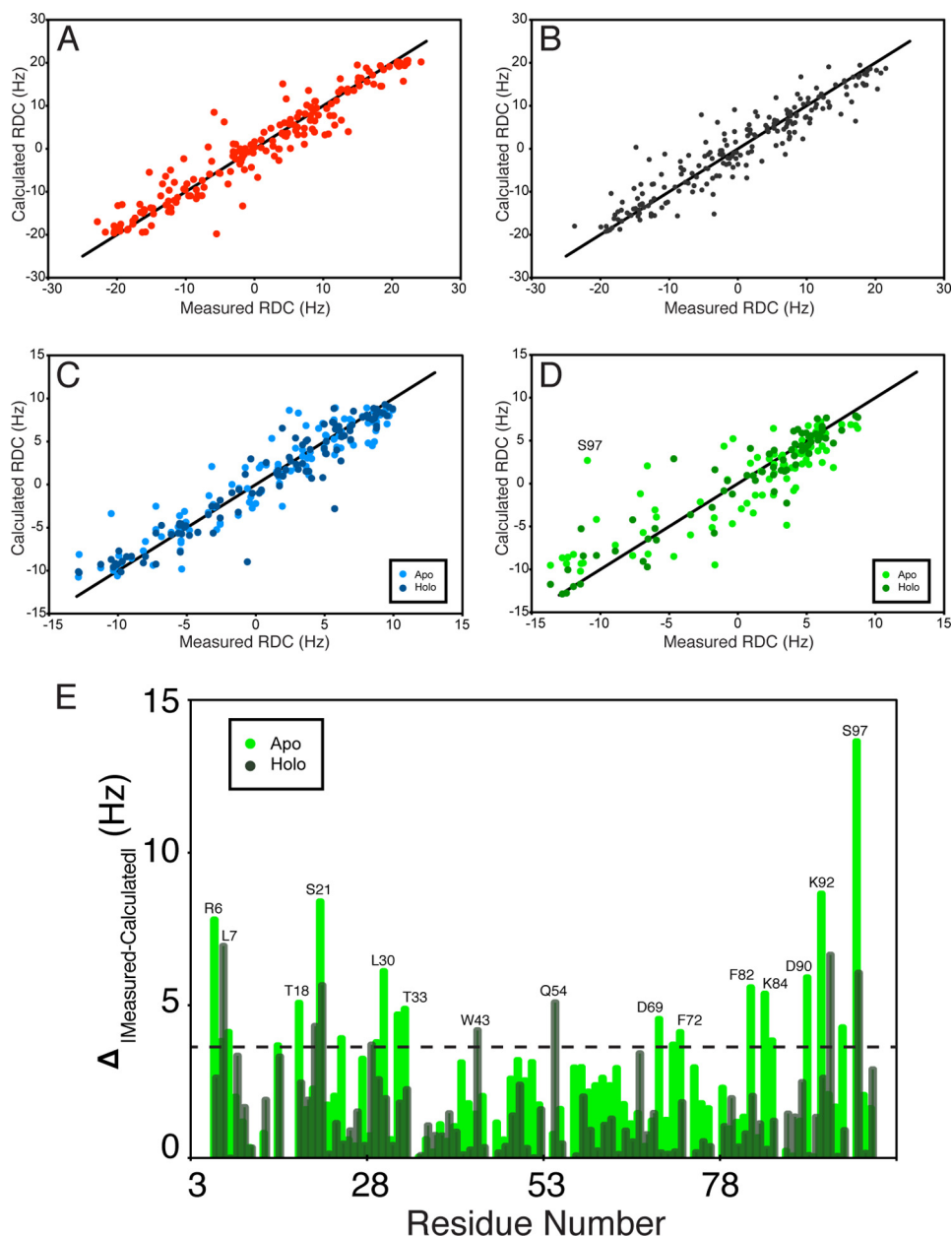
FIGURE 5. **Correlation between isolated D1 and D2 and their wild-type equivalents in apo- and holo-HisJ as revealed by RDC analysis.** *A,* high *R* and low *Q* values (see Table 2) were obtained from fitting apo-HisJ RDCs and the starting model used in the structure calculations (see "Experimental Procedures"). *B,* similarly, holo-HisJ RDCs were fit to the holo-HisJ crystal structure (PDB 1HSL). *C,* D1 could be fit to either the lowest energy apo-HisJ NMR structure and the holo-HisJ structure. *D,* isolated D2 shows a better correlation with its domain in holo-HisJ than with the apo-HisJ NMR structure. *E,* absolute value difference plot in measured and back-calculated RDCs between isolated D2 and the same domain in either the apo- or holo-HisJ structure is plotted as a function of D2 residue number, and outliers are indicated by the *horizontal line.*

residues experience significant CSPs when apo-HisJ is titrated with histidine; however, in the individual D1 titration, significant CSPs (>1 S.D.) for only Tyr-17, Ala-18, Ser-73, and Ser-75 were detected.

Interdomain Interactions—Analysis of the lowest energy apo-HisJ NMR structure and holo-HisJ crystal structure (PDB 1HSL) reveals that the number of residues making significant (>1 S.D.) contact area between the two protein lobes increases from 5 to 13, which results in an $\sim$2.4-fold increase in interdomain contact surface area (Table 3). Of these, important contributions are made from D1 residues 16–18 and 55 and 56, which contact D2 residues 121–123, 144–147, and 164–171 to help stabilize the closed holo-form.

NMR titrations were performed with D1 and D2 to examine the ability of the isolated domains to interact with each other. ^{15}N-D1 was titrated with unlabeled D2, and changes in peak position and intensity were monitored; however, no significant changes were observed (data not shown). Moreover, ^{15}N-D2 was titrated with unlabeled D1, and no significant changes were noted except for Asp-100, which lies at the C terminus of the D2 construct (data not shown). The addition of histidine to an equimolar mixture of ^{15}N-D1 and ^{15}N-D2 did not result in any significant chemical shifts (data not shown) apart from those observed from the ^{15}N-D1-histidine titration (Fig. 9, *A* and *B*). Similar to the D1-histidine ITC titration (data not shown), ITC experiments per-
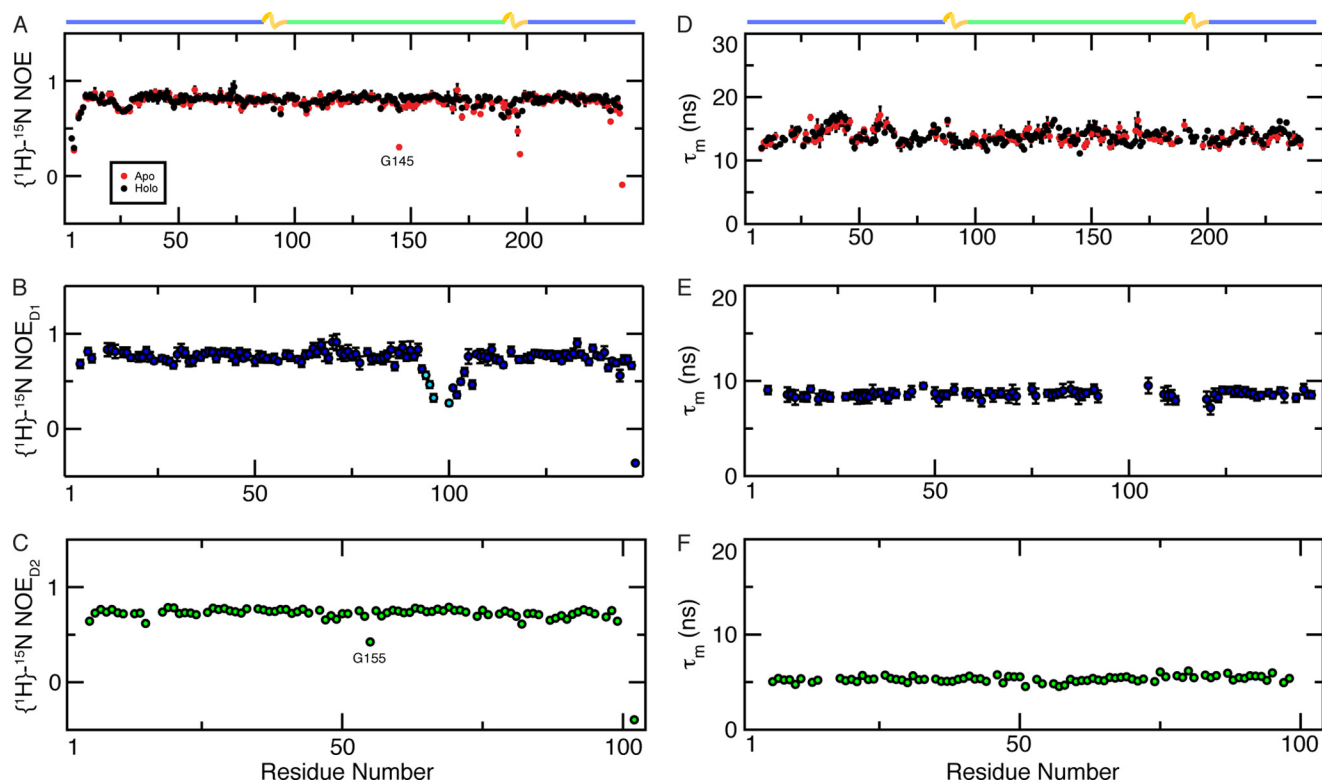
FIGURE 6. **NMR spin relaxation properties of the HisJ constructs used in this study.** $\{^1H\}$ ^{15}N NOE spin relaxation parameters and rotational correlation time for the global tumbling (τ_m) of each residue for apo- (*red*) and holo- (*black*) HisJ (*A* and *D*) and isolated D1 (*B* and *E*) and D2 (*C* and *F*). Of note, residues in the inserted flexible linker in D1 (*B*) are colored in *light blue*. The domain organization of HisJ is noted *above* the plots in *A* and *D*.
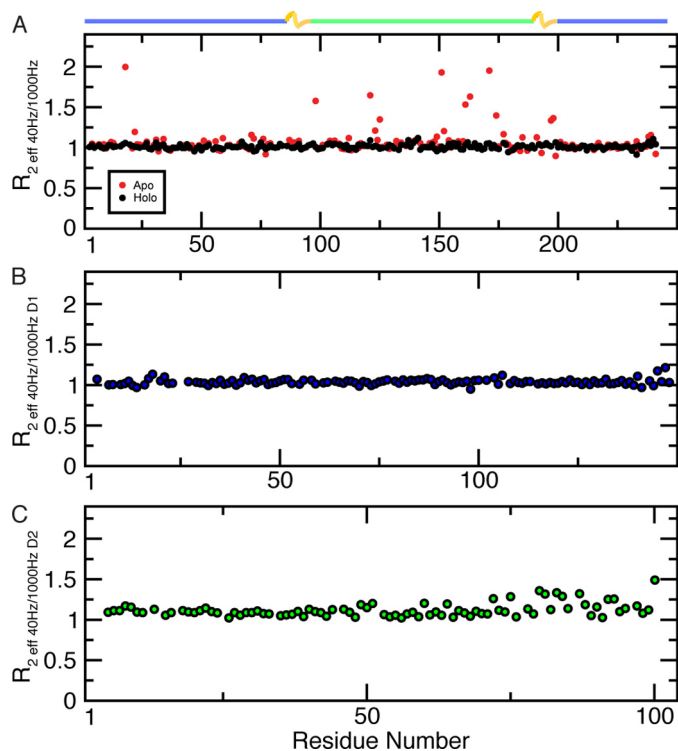

FIGURE 7. **Slow motion (millisecond to microsecond) dynamics from backbone CPMG experiments.** *A,* apo- and holo-HisJ are depicted in *red* and *black*, respectively. The isolated D1 (*blue*) (*B*) and D2 (*green*) (*C*) constructs are also shown. The $R_{2\,eff}$ ratio was calculated from experiments acquired at ν_{CPMG} of 40 and 1000 Hz and are plotted per residue.

formed on a 1:1 molar ratio of D1/D2 with histidine did not produce a detectable heat change (data not shown).

DISCUSSION

Dynamics of Ligand Binding—Our solution structure of apo-HisJ shows that it adopts an open conformation in the absence of ligand and that the ordering of dynamic residues in the hinge regions contributes to HisJ transitioning to a closed form in the presence of histidine (Fig. 3*B*). This large scale conformational change is reminiscent of the "Venus flytrap" mechanism of ligand binding used by other PBPs (65), such as LAOBP and maltose-binding protein (MBP). Although the apo-HisJ solution structure shows an average open conformation, we also present CPMG dynamics data that support a minor apo-conformation(s) based on an increase in chemical exchange for D2 (Fig. 7*A*). This result is corroborated by HisJ MD simulations that show that apo-HisJ is able to sample a closed conformation (66). Previous studies with the type I MBP revealed a minor (5%) apo-closed conformation that was identified and solved using RDC analysis in combination with paramagnetic relaxation enhancement (67). This minor MBP conformation has also been sampled by MD simulations (68), although other efforts have used a combined NMR and CS-Rosetta approach to identify these "invisible" protein states (69). In contrast, a minor apo-conformation was not detectable for the type II glutamine-binding protein (70), indicating that not all structurally related PBPs undergo an NMR identifiable conformational transition in the absence of ligand.

For HisJ, binding of ligand results in the formation of a stable closed conformation that is characterized by an ordering of
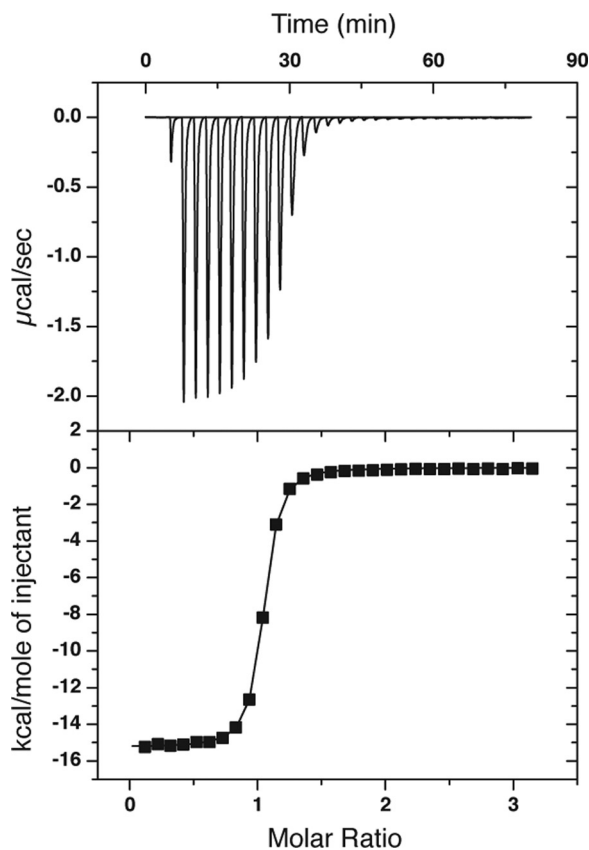
FIGURE 8. **Binding of histidine to HisJ by ITC.** A representative binding isotherm obtained by injecting histidine into apo-HisJ is shown.

FIGURE 9. **NMR titrations of histidine binding to ^{15}N-D1 (*A* and *B*) and ^{15}N-D2 (*C*).** *A*, region of the ^{15}N-D1 HSQC experiment. The majority of the peaks do not change position during the experiment; however, Ser-73 and Ser-75 shift steadily upon each addition (see *arrow*). *Inset* in *A* is the plot of Ser-73 peak position relative to histidine concentration and the K_d value as determined by the NMRViewJ titration analysis module (One Moon Scientific).

dynamic residues on both fast and slow NMR time scales. In comparison, the apo-form of the type II glutamine-binding protein has two rigid hinge strands that are stabilized by inter-hinge strand hydrogen bonds and whose residues are directly involved in ligand binding (70, 71). Tjandra and co-workers (70, 72) have suggested that variation in hinge flexibility among PBPs is related to ligand binding specificity and mediates the open-closed conformational transitions. Mutational studies of the interdomain hinge regions of the type I ribose-binding protein and glucose/galactose-binding protein have also been shown to alter hinge region dynamics and concomitantly the intrinsic binding affinity of these proteins for their ligands (73). Our results support an intimate role between hinge region dynamics and ligand binding in PBPs that is not dependent on contact between the hinge and ligand.

Multifunctional Roles of D1 and D2—In this study, the main polypeptide chain break points for our isolation of the individual D1 and D2 domains of HisJ were chosen to coincide with the hinge regions. RDC, CSI, CSP, dihedral angle backbone analysis, and NMR spin relaxation data indicate that these two isolated domains are folded similarly compared with their homologous domains in apo-HisJ, except for terminal regions and residues adjacent to the inserted flexible linker in D1. The other main structural differences originated in D2. CSP, RDC, and NMR relaxation dispersion data indicate two loop regions in D2 (residues 30–35 near α-helix 2 and 72–75 near α-helix 4) are significantly affected in the absence of intact interdomain linkers (Fig. 10, *A* and *B*).
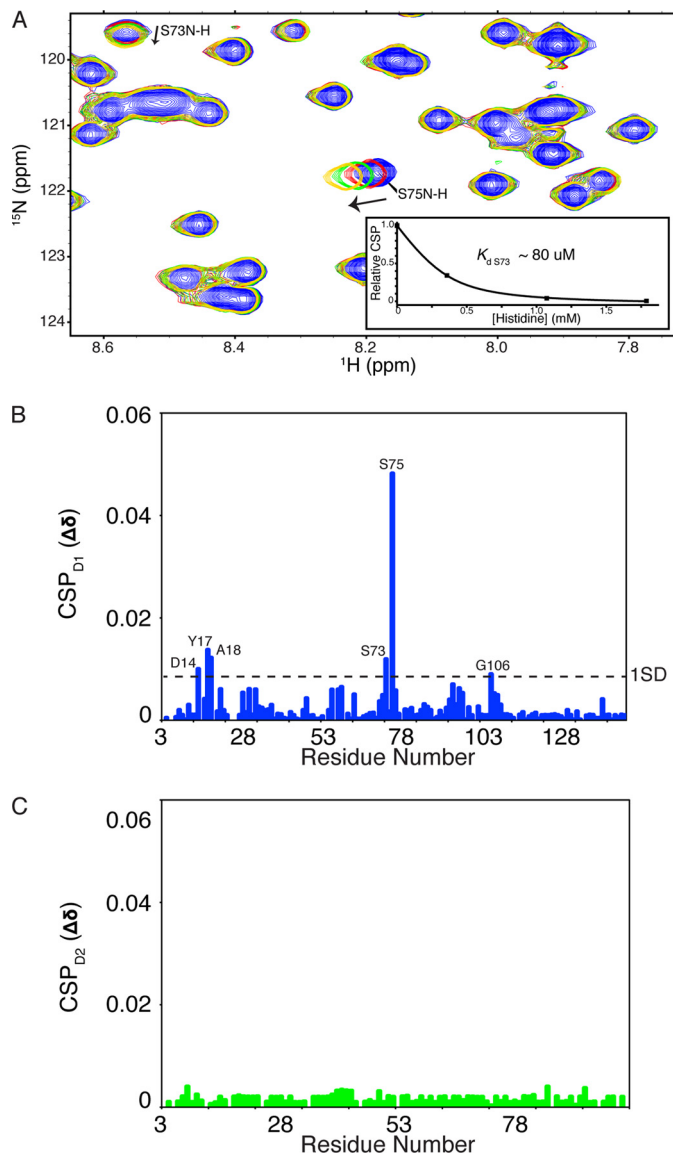
From the holo-HisJ crystal structure (PDB 1HSL), it is observed that the majority (~60%) of the direct contact surface area with histidine occurs through residues in the D1 domain. This has led to the idea that D1 and D2 may have different roles in PBP ligand binding (14), where D1 serves as the initial ligand acceptor. To date, experimental evidence to support such a model in PBPs is limited to the structure of the type I *E. coli* leucine, isoleucine, and valine-binding protein where leucine was soaked into the crystal and bound to D1 (PDB 2LIV) (74) and theoretical targeted MD simulations of the same protein (75). MD simulations of LAOBP also indicated that an initial D1-ligand contact step was required for an open-to-closed conformational change to occur (76). In this study, we provide direct experimental evidence that isolated D1 of HisJ, but not D2, is able to bind histidine in a similar manner as the full-

length HisJ. D1 residues Tyr-17, Ser-73, and Ser-75 show significant CSPs upon histidine titration. These residues along with Leu-55 and Ser-72, which also have high CSP values, comprise the histidine binding pocket of D1 (Fig. 9*B*). These affected residues are identical to those perturbed by addition of histidine to the full-length HisJ protein (Fig. 3*C*) and those that participate in histidine coordination in the in the holo-HisJ crystal structure. The ability of D1 to bind histidine supports a model where this domain is involved in the initial ligand binding step of HisJ and related proteins (*e.g.* LAOBP) (14, 24). Furthermore, the apparent reduced affinity of D1 for histidine is in

TABLE 3

Analysis of interdomain and interhinge strand contacts

Contact surface area was calculated using contact map analysis software (92).

Interaction partners	Residue (D1)	Residue (D2)	Contact surface area
			$Å^2$
Apo-HisJ			
D1–D2	19	170	39.6
	20	166	33.8
	234	166	24.2
	236	165	34.5
	236	166	28.9
Hinge 1–hinge 2	194	93	33.5
Holo-HisJ			
D1–D2	16	146	32.7
	16	147	23.2
	17	167	42.9
	17	164	31.8
	17	146	28.9
	18	171	25.4
	19	170	27.9
	55	123	24.4
	56	121	36.9
	56	144	35.4
	234	166	32.3
	236	166	23.1
	236	170	27.3
Hinge 1–Hinge 2	194	95	32.6
D1/D2–histidine	17		48.1
	55		18.1
	72		21.7
	73		32
	75		30.6
	80		31.6
		120	19.6
		123	21
		124	42.8
		125	21
		146 (H$_2$O-mediated)	0.6
		164	26.8

agreement with the notion that a D2 interaction is required to further increase the affinity of HisJ for its ligand.

The inability of isolated D2 to interact with histidine indicates that it plays a supporting role in ligand binding. Previous studies have proposed that PBP-ligand binding occurs by an induced-fit mechanism wherein domain closure is stimulated by a ligand binding event (14, 21, 24, 70, 77, 78). In the case of HisJ, we suggest that histidine binding at D1 triggers a closing event that rapidly brings D2 in close proximity with D1. In the absence of interdomain connectivity, D2 is unable to make contact with the ligand; D1 and D2 are not able to interact; and a conformational change leading to a closed holo-form is not communicated.
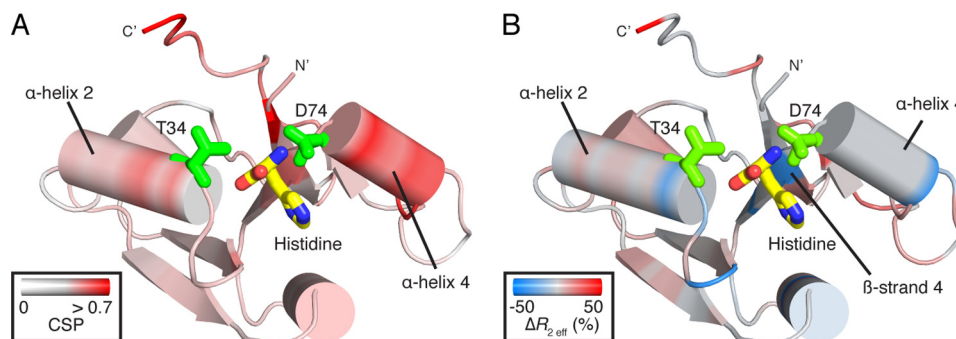
The changes in chemical environment and structure of D2 loop regions (residues 30–35 and 72–75) in the absence of interdomain connectivity directly affects residues involved in both ligand binding and domain-domain contacts (Fig. 10*A*). Similarly, a loss in R_2 chemical exchange for residues 31, 35, 71, and 73 in isolated D2 agrees with this notion (Fig. 10*B*). Previous studies have shown that mutations to Thr-34 (full-length T124A) and Asp-74 (D164A/E165K) reduce HisJ binding affinity for histidine by >150-fold (24, 64, 79). Moreover, a T124A HisJ mutant was unable to form a stable, closed-liganded conformation (64). Mutations to other residues in the same D2 loop regions have also been shown to disrupt histidine binding and the ability to adopt a closed conformation (64). In particular, our analysis reveals that loop residues 72–75 and the proceeding α-helix 4 of D2 are extensively involved in making interdomain contacts in both apo- and holo-HisJ (Table 3). This indicates that in the absence of intact hinge regions, chemical environmental changes in D2 affect the ability of this domain to interact with ligand and D1. In this regard, mutation of S95F from the 1st hinge strand has been previously shown to affect the ability of HisJ to bind histidine (K_d >5 μM) and adopt a closed conformation (24).

Currently, the body of information regarding the interaction of PBPs and their inner membrane ABC transporters is growing (80, 81). Studies involving MBP and its ABC transporter MalFGK$_2$ have established that a large extracellular loop (MalF-P2) is responsible for mediating interactions with MBP and inducing a conformational change that leads to release of its ligand (82–87). Previous work by Ames and co-workers

FIGURE 10. **Mapping of CSPs (*A*) and changes in $R_{2\ eff}$ chemical exchange (*B*) onto the D2 structure from holo-HisJ.** *A*, CSPs arise from differences in isolated D2 and the same domain in apo-HisJ. Significant changes (indicated in *red*) are localized near α-helix 2 and 4, and key ligand-binding residues (*green*) Thr-34 (full-length Thr-124) and Asp-74 (full-length Asp-164) are indicated. *B*, relative change in $R_{2\ eff\ (D2-apo)}$ (%) where loss and gain in chemical exchange of D2 compared with apo-HisJ are indicated in *blue* and *red*, respectively. Significant decreases in $R_{2\ eff}$ are found near residue Thr-34 and adjacent to Asp-74 on β-strand 4.

(88–90) has established that HisJ docks onto HisQMP$_2$, and mutational studies have shown that regions on D1 and D2 have a role in forming a stable complex with the permease and in signaling active transport of the ligand. HisQMP$_2$ is not predicted to have a large periplasmic signaling loop (91); thus, it remains to be established what the molecular mechanism is that induces ligand release from PBPs with transporters that lack large extracellular loops. Our study with the individual lobes of HisJ suggests that a change in PBP conformation that separates the two lobes would significantly weaken the association with the ligand and could facilitate ligand release. A ligand-dependent transport rate for HisQMP$_2$ has also been observed, but the biochemical nature of this regulation has not been elucidated (21). Future solution NMR studies of HisJ bound to other basic amino acids (*i.e.* arginine, ornithine, and lysine) may show differences that are not apparent from the crystal structures of holo-LAOBP (PDB 1LAH, 1LAG, 1LAF, and 1LST). Moreover, it is unclear if both lobes of HisJ are required to stimulate transport, which could be studied using the isolated domain constructs described in this work.

This HisJ study is the first to structurally and functionally characterize the individual lobes of a PBP. We have also attempted to perform similar studies for PBPs that have a single hinge region (ferric enterobactin-binding protein) and three hinge regions (MBP) but have not yet been successful.[3]

REFERENCES

1. Ames, G. F., and Lever, J. (1970) Components of histidine transport: histidine-binding proteins and HisP protein. *Proc. Natl. Acad. Sci. U.S.A.* **66,** 1096–1103
2. Nossal, N. G., and Heppel, L. A. (1966) The release of enzymes by osmotic shock from *Escherichia coli* in exponential phase. *J. Biol. Chem.* **241,** 3055–3062
3. Brown, K. D. (1970) Formation of aromatic amino acid pools in *Escherichia coli* K-12. *J. Bacteriol.* **104,** 177–188
4. Doige, C. A., and Ames, G. F. (1993) ATP-dependent transport systems in bacteria and humans: relevance to cystic fibrosis and multidrug resistance. *Annu. Rev. Microbiol.* **47,** 291–319
5. Ames, G. F., and Lever, J. E. (1972) The histidine-binding protein J is a component of histidine transport. Identification of its structural gene, *hisJ*. *J. Biol. Chem.* **247,** 4309–4316
6. Lever, J. E. (1972) Quantitative assay of the binding of small molecules to protein: comparison of dialysis and membrane filter assays. *Anal. Biochem.* **50,** 73–83
7. Nikaido, K., and Ames, G. F. (1992) Purification and characterization of the periplasmic lysine-, arginine-, ornithine-binding protein (LAO) from *Salmonella typhimurium*. *J. Biol. Chem.* **267,** 20706–20712
8. Lee, Y. H., Deka, R. K., Norgard, M. V., Radolf, J. D., and Hasemann, C. A. (1999) *Treponema pallidum* TroA is a periplasmic zinc-binding protein with a helical backbone. *Nat. Struct. Biol.* **6,** 628–633
9. Quiocho, F. A., and Ledvina, P. S. (1996) Atomic structure and specificity of bacterial periplasmic receptors for active transport and chemotaxis: variation of common themes. *Mol. Microbiol.* **20,** 17–25
10. Chu, B. C., and Vogel, H. J. (2011) A structural and functional analysis of type III periplasmic and substrate binding proteins: their role in bacterial siderophore and heme transport. *Biol. Chem.* **392,** 39–52
11. Claverys, J. P. (2001) A new family of high-affinity ABC manganese and zinc permeases. *Res. Microbiol.* **152,** 231–243
12. Tam, R., and Saier, M. H., Jr. (1993) Structural, functional, and evolutionary relationships among extracellular solute-binding receptors of bacteria. *Microbiol. Rev.* **57,** 320–346
13. Krewulak, K. D., Peacock, R. S., and Vogel, H. J. (2004) in *Periplasmic Binding Proteins Involved in Bacterial Iron Uptake* (Crosa, J. H., Mey, A. R., and Payne, S. M., eds) pp. 113–129, American Society for Microbiology, Washington, D. C.
14. Oh, B. H., Pandit, J., Kang, C. H., Nikaido, K., Gokcen, S., Ames, G. F., and Kim, S. H. (1993) Three-dimensional structures of the periplasmic lysine/arginine/ornithine-binding protein with and without a ligand. *J. Biol. Chem.* **268,** 11348–11355
15. Hsiao, C. D., Sun, Y. J., Rose, J., and Wang, B. C. (1996) The crystal structure of glutamine-binding protein from *Escherichia coli*. *J. Mol. Biol.* **262,** 225–242
16. Kang, C. H., Shin, W. C., Yamagata, Y., Gokcen, S., Ames, G. F., and Kim, S. H. (1991) Crystal structure of the lysine-, arginine-, ornithine-binding protein (LAO) from *Salmonella typhimurium* at 2.7-Å resolution. *J. Biol. Chem.* **266,** 23893–23899
17. Sun, Y. J., Rose, J., Wang, B. C., and Hsiao, C. D. (1998) The structure of glutamine-binding protein complexed with glutamine at 1.94 Å resolution: comparisons with other amino acid-binding proteins. *J. Mol. Biol.* **278,** 219–229
18. Cedel, T. E., Cottam, P. F., Meadows, M. D., and Ho, C. (1984) A high-resolution ^{1}H-NMR investigation of the histidine-binding protein J of *Salmonella typhimurium*. Substrate-induced conformational changes. *Biophys. Chem.* **19,** 279–287
19. Post, J. F., Cottam, P. F., Simplaceanu, V., and Ho, C. (1984) Fluorine-19 nuclear magnetic resonance study of 5-fluorotryptophan-labeled histidine-binding protein J of *Salmonella typhimurium*. *J. Mol. Biol.* **179,** 729–743
20. Zukin, R. S., Klos, M. F., and Hirsch, R. E. (1986) Conformational dynamics of two histidine-binding proteins of *Salmonella typhimurium*. *Biophys. J.* **49,** 1229–1235
21. Wolf, A., Lee, K. C., Kirsch, J. F., and Ames, G. F. (1996) Ligand-dependent conformational plasticity of the periplasmic histidine-binding protein HisJ. Involvement in transport specificity. *J. Biol. Chem.* **271,** 21243–21250
22. Wolf, A., Shaw, E. W., Nikaido, K., and Ames, G. F. (1994) The histidine-binding protein undergoes conformational changes in the absence of ligand as analyzed with conformation-specific monoclonal antibodies. *J. Biol. Chem.* **269,** 23051–23058
23. Yao, N., Trakhanov, S., and Quiocho, F. A. (1994) Refined 1.89-Å structure of the histidine-binding protein complexed with histidine and its relationship with many other active transport/chemosensory proteins. *Biochemistry* **33,** 4769–4779
24. Oh, B. H., Kang, C. H., De Bondt, H., Kim, S. H., Nikaido, K., Joshi, A. K., and Ames, G. F. (1994) The bacterial periplasmic histidine-binding protein. Structure/function analysis of the ligand-binding site and comparison with related proteins. *J. Biol. Chem.* **269,** 4135–4143
25. Tugarinov, V., Kanelis, V., and Kay, L. E. (2006) Isotope labeling strategies for the study of high-molecular-weight proteins by solution NMR spectroscopy. *Nat. Protoc.* **1,** 749–754
26. Huang, H., and Vogel, H. J. (2013) Purification and stable isotope-labeling of calcium-and integrin-binding protein 1 for structural and functional NMR studies. *Methods Mol. Biol.* **963,** 99–113
27. Bradford, M. M. (1976) A rapid and sensitive method for the quantitation of microgram quantities of protein utilizing the principle of protein-dye binding. *Anal. Biochem.* **72,** 248–254
28. Otten, R., Chu, B., Krewulak, K. D., Vogel, H. J., and Mulder, F. A. (2010) Comprehensive and cost-effective NMR spectroscopy of methyl groups in large proteins. *J. Am. Chem. Soc.* **132,** 2952–2960
29. Eletsky, A., Kienhöfer, A., and Pervushin, K. (2001) TROSY NMR with partially deuterated proteins. *J. Biomol. NMR* **20,** 177–180
30. Salzmann, M., Wider, G., Pervushin, K., Senn, H., and Wuthrich, K. (1999) TROSY-type triple resonance experiments for sequential NMR assign-

ments of large proteins. *J. Am. Chem. Soc.* **121,** 844–848

31. Farrow, N. A., Muhandiram, R., Singer, A. U., Pascal, S. M., Kay, C. M., Gish, G., Shoelson, S. E., Pawson, T., Forman-Kay, J. D., and Kay, L. E. (1994) Backbone dynamics of a free and a phosphopeptide-complexed Src homology 2 domain studied by ^{15}N NMR relaxation. *Biochemistry* **33,** 5984–6003

32. Loria, J. P., Rance, M., and Palmer, A. G., 3rd (1999) A TROSY CPMG sequence for characterizing chemical exchange in large proteins. *J. Biomol. NMR* **15,** 151–155

33. Mulder, F. A., Mittermaier, A., Hon, B., Dahlquist, F. W., and Kay, L. E. (2001) Studying excited states of proteins by NMR spectroscopy. *Nat. Struct. Biol.* **8,** 932–935

34. Zhu, G., Kong, X. M., and Sze, K. H. (1999) Gradient and sensitivity enhancement of 2D TROSY with water flip-back, 3D NOESY-TROSY and TOCSY-TROSY experiments. *J. Biomol. NMR* **13,** 77–81

35. Orekhov, V. Y., Ibraghimov, I., and Billeter, M. (2003) Optimizing resolution in multidimensional NMR by three-way decomposition. *J. Biomol. NMR* **27,** 165–173

36. Hansen, M. R., Mueller, L., and Pardi, A. (1998) Tunable alignment of macromolecules by filamentous phage yields dipolar coupling interactions. *Nat. Struct. Biol.* **5,** 1065–1074

37. Ottiger, M., Delaglio, F., and Bax, A. (1998) Measurement of J and dipolar couplings from simplified two-dimensional NMR spectra. *J. Magn. Reson.* **131,** 373–378

38. Zweckstetter, M., and Bax, A. (2000) Prediction of sterically induced alignment in a dilute liquid crystalline phase: aid to protein structure determination by NMR. *J. Am. Chem. Soc.* **122,** 3791–3792

39. Eswar, N., John, B., Mirkovic, N., Fiser, A., Ilyin, V. A., Pieper, U., Stuart, A. C., Marti-Renom, M. A., Madhusudhan, M. S., Yerkovich, B., and Sali, A. (2003) Tools for comparative protein structure modeling and analysis. *Nucleic Acids Res.* **31,** 3375–3380

40. Mulder, F. A., Schipper, D., Bott, R., and Boelens, R. (1999) Altered flexibility in the substrate-binding site of related native and engineered high-alkaline *Bacillus subtilisins*. *J. Mol. Biol.* **292,** 111–123

41. Delaglio, F., Grzesiek, S., Vuister, G. W., Zhu, G., Pfeifer, J., and Bax, A. (1995) NMRPipe: a multidimensional spectral processing system based on UNIX pipes. *J. Biomol. NMR* **6,** 277–293

42. Goddard, T. D., and Kneller, D. G. (2003) *Sparky 3*, Version 3.113, University of California, San Francisco

43. Shen, Y., Delaglio, F., Cornilescu, G., and Bax, A. (2009) TALOS+: a hybrid method for predicting protein backbone torsion angles from NMR chemical shifts. *J. Biomol. NMR* **44,** 213–223

44. Wishart, D. S., Bigam, C. G., Yao, J., Abildgaard, F., Dyson, H. J., Oldfield, E., Markley, J. L., and Sykes, B. D. (1995) ^{1}H, ^{13}C and ^{15}N chemical shift referencing in biomolecular NMR. *J. Biomol. NMR* **6,** 135–140

45. Mosteller, F., and Tukey, J. W. (1977) *Data Analysis and Regression: A Second Course in Statistics*, pp. 133–163, Addison-Wesley, Reading, MA

46. Barbato, G., Ikura, M., Kay, L. E., Pastor, R. W., and Bax, A. (1992) Backbone dynamics of calmodulin studied by ^{15}N relaxation using inverse detected two-dimensional NMR spectroscopy: the central helix is flexible. *Biochemistry* **31,** 5269–5278

47. Guex, N., and Peitsch, M. C. (1997) SWISS-MODEL and the Swiss-Pdb-Viewer: an environment for comparative protein modeling. *Electrophoresis* **18,** 2714–2723

48. Gardner, K. H., Rosen, M. K., and Kay, L. E. (1997) Global folds of highly deuterated methyl-protonated proteins by multidimensional NMR. *Biochemistry* **36,** 1389–1401

49. Venters, R. A., Farmer, B. T., 2nd, Fierke, C. A., and Spicer, L. D. (1996) Characterizing the use of perdeuteration in NMR studies of large proteins. *J. Mol. Biol.* **264,** 1101–1116

50. Wishart, D. S., and Sykes, B. D. (1994) The ^{13}C chemical-shift index: a simple method for the identification of protein secondary structure using ^{13}C chemical-shift data. *J. Biomol. NMR* **4,** 171–180

51. Tugarinov, V., Choy, W. Y., Orekhov, V. Y., and Kay, L. E. (2005) Solution NMR-derived global fold of a monomeric 82-kDa enzyme. *Proc. Natl. Acad. Sci. U.S.A.* **102,** 622–627

52. Tjandra, N., Omichinski, J. G., Gronenborn, A. M., Clore, G. M., and Bax, A. (1997) Use of dipolar ^{1}H-^{15}N and ^{1}H-^{13}C couplings in the structure determination of magnetically oriented macromolecules in solution. *Nat. Struct. Biol.* **4,** 732–738

53. Tolman, J. R., Flanagan, J. M., Kennedy, M. A., and Prestegard, J. H. (1995) Nuclear magnetic dipole interactions in field-oriented proteins: information for structure determination in solution. *Proc. Natl. Acad. Sci. U.S.A.* **92,** 9279–9283

54. Schwieters, C. D., Kuszewski, J. J., Tjandra, N., and Clore, G. M. (2003) The Xplor-NIH NMR molecular structure determination package. *J. Magn. Reson.* **160,** 65–73

55. Chou, J. J., Li, S., and Bax, A. (2000) Study of conformational rearrangement and refinement of structural homology models by the use of heteronuclear dipolar couplings. *J. Biomol. NMR* **18,** 217–227

56. Gifford, J. L., Ishida, H., and Vogel, H. J. (2011) Fast methionine-based solution structure determination of calcium-calmodulin complexes. *J. Biomol. NMR* **50,** 71–81

57. Huang, H., and Vogel, H. J. (2012) Structural basis for the activation of platelet integrin αIIbβ3 by calcium- and integrin-binding protein 1. *J. Am. Chem. Soc.* **134,** 3864–3872

58. Bhattacharya, A., Tejero, R., and Montelione, G. T. (2007) Evaluating protein structures determined by structural genomics consortia. *Proteins* **66,** 778–795

59. DeLano, W. L. (2010) *The PyMOL Molecular Graphics System*, Version 1.3r1, Schrödinger, LLC, New York

60. Igarashi, S., Osawa, M., Ozawa, S., and Shimada, I. (2010) Backbone resonance assignments for the ligand binding subunit of the histidine permease complex (HisJ) from *Escherichia coli*, under histidine-bound and unbound states. *Biomol. NMR Assign.* **4,** 17–20

61. Fukami-Kobayashi, K., Tateno, Y., and Nishikawa, K. (1999) Domain dislocation: a change of core structure in periplasmic binding proteins in their evolutionary history. *J. Mol. Biol.* **286,** 279–290

62. Tjandra, N., and Bax, A. (1997) Direct measurement of distances and angles in biomolecules by NMR in a dilute liquid crystalline medium. *Science* **278,** 1111–1114

63. Miller, D. M., 3rd, Olson, J. S., Pflugrath, J. W., and Quiocho, F. A. (1983) Rates of ligand binding to periplasmic proteins involved in bacterial transport and chemotaxis. *J. Biol. Chem.* **258,** 13665–13672

64. Wolf, A., Shaw, E. W., Oh, B. H., De Bondt, H., Joshi, A. K., and Ames, G. F. (1995) Structure/function analysis of the periplasmic histidine-binding protein. Mutations decreasing ligand binding alter the properties of the conformational change and of the closed form. *J. Biol. Chem.* **270,** 16097–16106

65. Felder, C. B., Graul, R. C., Lee, A. Y., Merkle, H. P., and Sadee, W. (1999) The Venus flytrap of periplasmic binding proteins: an ancient protein module present in multiple drug receptors. *AAPS PharmSci.* **1,** E2

66. Chu, B. C., Chan, D. I., DeWolf, T., Periole, X., and Vogel, H. J. (2013) Molecular dynamics simulations reveal that Apo-HisJ can sample a closed conformation. *Proteins* 10.1002/prot.24396

67. Tang, C., Schwieters, C. D., and Clore, G. M. (2007) Open-to-closed transition in apo maltose-binding protein observed by paramagnetic NMR. *Nature* **449,** 1078–1082

68. Bucher, D., Grant, B. J., Markwick, P. R., and McCammon, J. A. (2011) Accessing a hidden conformation of the maltose binding protein using accelerated molecular dynamics. *PLoS Comput. Biol.* **7,** e1002034

69. Korzhnev, D. M., Religa, T. L., Banachewicz, W., Fersht, A. R., and Kay, L. E. (2010) A transient and low-populated protein-folding intermediate at atomic resolution. *Science* **329,** 1312–1316

70. Bermejo, G. A., Strub, M. P., Ho, C., and Tjandra, N. (2010) Ligand-free open-closed transitions of periplasmic binding proteins: the case of glutamine-binding protein. *Biochemistry* **49,** 1893–1902

71. Bermejo, G. A., Strub, M. P., Ho, C., and Tjandra, N. (2009) Determination of the solution-bound conformation of an amino acid binding protein by NMR paramagnetic relaxation enhancement: use of a single flexible paramagnetic probe with improved estimation of its sampling space. *J. Am. Chem. Soc.* **131,** 9532–9537

72. Pistolesi, S., Tjandra, N., and Bermejo, G. A. (2011) Solution NMR studies of periplasmic binding proteins and their interaction partners. *Biomol. Concepts* **2,** 53–64

73. Ortega, G., Castaño, D., Diercks, T., and Millet, O. (2012) Carbohydrate

affinity for the glucose-galactose binding protein is regulated by allosteric domain motions. *J. Am. Chem. Soc.* **134,** 19869–19876

74. Sack, J. S., Saper, M. A., and Quiocho, F. A. (1989) Periplasmic binding protein structure and function. Refined x-ray structures of the leucine/isoleucine/valine-binding protein and its complex with leucine. *J. Mol. Biol.* **206,** 171–191

75. Trakhanov, S., Vyas, N. K., Luecke, H., Kristensen, D. M., Ma, J., and Quiocho, F. A. (2005) Ligand-free and -bound structures of the binding protein (LivJ) of the *Escherichia coli* ABC leucine/isoleucine/valine transport system: trajectory and dynamics of the interdomain rotation and ligand specificity. *Biochemistry* **44,** 6597–6608

76. Silva, D. A., Domínguez-Ramírez, L., Rojo-Domínguez, A., and Sosa-Peinado, A. (2011) Conformational dynamics of L-lysine, L-arginine, L-ornithine binding protein reveals ligand-dependent plasticity. *Proteins* **79,** 2097–2108

77. Ames, G. F. (1986) Bacterial periplasmic transport systems: structure, mechanism, and evolution. *Annu. Rev. Biochem.* **55,** 397–425

78. Stockner, T., Vogel, H. J., and Tieleman, D. P. (2005) A salt-bridge motif involved in ligand binding and large-scale domain motions of the maltose-binding protein. *Biophys. J.* **89,** 3362–3371

79. Prossnitz, E. (1991) Determination of a region of the HisJ binding protein involved in the recognition of the membrane complex of the histidine transport system of *Salmonella typhimurium. J. Biol. Chem.* **266,** 9673–9677

80. Schneider, E., Eckey, V., Weidlich, D., Wiesemann, N., Vahedi-Faridi, A., Thaben, P., and Saenger, W. (2012) Receptor-transporter interactions of canonical ATP-binding cassette import systems in prokaryotes. *Eur. J. Cell Biol.* **91,** 311–317

81. Locher, K. P. (2009) Structure and mechanism of ATP-binding cassette transporters. *Philos. Trans. R. Soc. Lond. B Biol. Sci.* **364,** 239–245

82. Böhm, S., Licht, A., Wuttge, S., Schneider, E., and Bordignon, E. (2013) Conformational plasticity of the type I maltose ABC importer. *Proc. Natl. Acad. Sci. U.S.A.* **110,** 5492–5497

83. Daus, M. L., Grote, M., and Schneider, E. (2009) The MalF P2 loop of the ATP-binding cassette transporter MalFGK2 from *Escherichia coli* and *Salmonella enterica* serovar *typhimurium* interacts with maltose binding protein (MalE) throughout the catalytic cycle. *J. Bacteriol.* **191,** 754–761

84. Jacso, T., Grote, M., Daus, M. L., Schmieder, P., Keller, S., Schneider, E., and Reif, B. (2009) Periplasmic loop P2 of the MalF subunit of the maltose ATP binding cassette transporter is sufficient to bind the maltose binding protein MalE. *Biochemistry* **48,** 2216–2225

85. Jacso, T., Schneider, E., Rupp, B., and Reif, B. (2012) Substrate transport activation is mediated through second periplasmic loop of transmembrane protein MalF in maltose transport complex of *Escherichia coli. J. Biol. Chem.* **287,** 17040–17049

86. Oldham, M. L., and Chen, J. (2011) Snapshots of the maltose transporter during ATP hydrolysis. *Proc. Natl. Acad. Sci. U.S.A.* **108,** 15152–15156

87. Oldham, M. L., and Chen, J. (2011) Crystal structure of the maltose transporter in a pretranslocation intermediate state. *Science* **332,** 1202–1205

88. Ames, G. F., and Spurich, E. N. (1976) Protein-protein interaction in transport: periplasmic histidine-binding protein J interacts with P protein. *Proc. Natl. Acad. Sci. U.S.A.* **73,** 1877–1881

89. Prossnitz, E., Nikaido, K., Ulbrich, S. J., and Ames, G. F. (1988) Formaldehyde and photoactivatable cross-linking of the periplasmic binding protein to a membrane component of the histidine transport system of *Salmonella typhimurium. J. Biol. Chem.* **263,** 17917–17920

90. Liu, C. E., Liu, P. Q., Wolf, A., Lin, E., and Ames, G. F. (1999) Both lobes of the soluble receptor of the periplasmic histidine permease, an ABC transporter (traffic ATPase), interact with the membrane-bound complex. Effect of different ligands and consequences for the mechanism of action. *J. Biol. Chem.* **274,** 739–747

91. Eckey, V., Weidlich, D., Landmesser, H., Bergmann, U., and Schneider, E. (2010) The second extracellular loop of pore-forming subunits of ATP-binding cassette transporters for basic amino acids plays a crucial role in interaction with the cognate solute binding protein(s). *J. Bacteriol.* **192,** 2150–2159

92. Sobolev, V., Eyal, E., Gerzon, S., Potapov, V., Babor, M., Prilusky, J., and Edelman, M. (2005) SPACE: a suite of tools for protein structure prediction and analysis based on complementarity and environment. *Nucleic Acids Res.* **33,** W39–W43